Yan Zhan
Department of Mechanical Engineering,
Stony Brook University,
Stony Brook, NY 11794

Foluso Ladeinde
Department of Mechanical Engineering,
Stony Brook University,
Stony Brook, NY 11794

Harold G. Kirk
Department of Physics,
Brookhaven National Laboratory,
Upton, NY 11973

Kirk T. McDonald
Department of Physics,
Princeton University,
Princeton, NJ 08544

The Effects of Pipe Geometry on Fluid Flow in a Muon Collider Particle Production System

Liquid mercury has been investigated as a potential high-Z target for the production of muon particles for the Muon Collider project. This paper investigates the dynamics of mercury flow in a design of the target delivery system, with the objective of determining pipe configurations that yield weak turbulence intensities at the exit of the pipe. Eight curved pipe geometries with various half-bend angles and with/without nozzles in the exit region are studied. A theoretical analysis is carried out for steady laminar incompressible flow, whereby the terms representing the curvature effects are examined. Subsequent simulations of the turbulent flow regime in the pipes are based on a realizable $k - \varepsilon$ Reynolds-Averaged Navier–Stokes (RANS) equations approach. The effects of half-bend angles and the presence of a nozzle on the momentum thickness and turbulence intensity at the exit plane of the curved pipe are discussed, as are the implications for the target delivery pipe designs. [DOI: 10.1115/1.4027176]

1 Introduction

The MERIT experiment at CERN [1,2] is a proof-of-principle test for a target system that converts a 4MW proton beam into a high-intensity muon beam for either a neutrino factory complex or a muon collider (see Fig. 1). The mercury jet issues from the nozzle at the end of a delivery pipe to form a target that intercepts an intense proton beam inside a 15T solenoid magnet. The use of liquid targets overcomes the problematic effects of solid targets such as the melting/vaporization of components, damage by beam-induced pressure waves for pulsed beams, and extensive radiation damage. Additionally, liquid target systems offer the advantage of the continuous regeneration of the target volume. However, the design of the mercury delivery pipe introduces new challenges.

The MERIT experiment uses a 180 deg bend, which has half-bend angles of 90 deg in the shape of a "U" for the delivery of the mercury. This geometry complicates the flow relative to that in a straight pipe and, arguably, affects the quality of the jet. Since the quality of the jet greatly influences the production of muon particles, it is pertinent to investigate the dynamics of the flow of mercury in the 180 deg bend, with a focus on the exit-flow results. Furthermore, for optimum muon particle production, the mercury flow should be near laminar. Four half-bend angles of 0 deg 30 deg 60 deg, and 90 deg have been chosen for investigation in this paper. For each configuration, a pipe with/without a nozzle is studied.

Eustice [3,4] is among the first to demonstrate the existence of a secondary flow in a curved pipe, an observation he made from injecting ink into water flowing through a pipe. Dean [5,6] introduces a parameter which bears his name (Dean number, $\mathrm{De} \equiv \mathrm{Re}\delta^{1/2}$, where Re is the Reynolds number based on the area-averaged mean velocity through a pipe of diameter $2a$ and δ is the curvature ratio ($\delta \equiv a/R$, where R is radius of curvature) used to characterize the magnitude and shape of the secondary motion inside a loosely coiled pipe ($\delta \ll 1$). Subsequent work by others have investigated curved pipes with different values of R. Adler [7] presents the experimental results of laminar and turbulent flows in three pipes with different R values. Rowe [8] investigates turbulent water flows for a curvature ratio of $\delta = 1/24$ in a circular 180 deg bend. The total pressure and yaw angle relative to the bend axis are measured for the Reynolds number Re $= 236,000$. Enayat et al. [9] reports on the axial components of the mean and fluctuating velocities for the turbulent water flow in a circular 90 deg bend for a δ value of $1/5.6$ and for a wide range of Reynolds numbers. Azzola et al. [10] computes and measures the developed turbulent flow in a 180 deg bend for $\delta = 1/6.75$ and Re $= 57,400$ and 110,000, using the standard $k - \varepsilon$ model. Answer et al. [11] measures the Reynolds stresses and mean velocity components in vertical and horizontal planes containing the pipe axis for air flow in a 180 deg bend, with $\delta = 1/13$ and Re $= 50,000$. Sudo et al. [12] reports on the measurements of the turbulent flow through a circular 90 deg bend with $\delta = 1/4$. Sudo and co-workers [13] also measure turbulent air flow in a 180 deg circular bend for the same δ value, but with Re $= 60,000$. The axial, radial, and circumferential components of the mean velocity and the corresponding components of the Reynolds stress tensor are reported. Hüttl et al. [14] investigate the influence of curvature and torsion on the turbulent flow in helically-coiled pipes for $\mathrm{Re}_\tau = 230$, where Re_τ is the mean friction velocity (u_τ)-based Reynolds number. The pipe curvature is found to induce a secondary flow with a strong effect on the fluid dynamics. Rudolf et al. [15] study the flow characteristics in several curved ducts: a single elbow to coupled elbows in the shapes of "U," "S." and the spatial right angle position, for a fixed value of $\delta = 1/4$ and Re $= 60,000$.
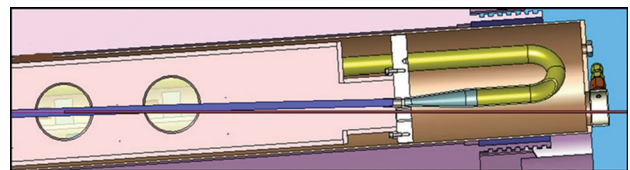
Fig. 1 Sectional view of the target supply pipe of the MERIT experiment. The mercury jet generated at the end of the nozzle is on top of the nominal beam trajectory (both the mercury jet and proton beam move from right to left in this figure).
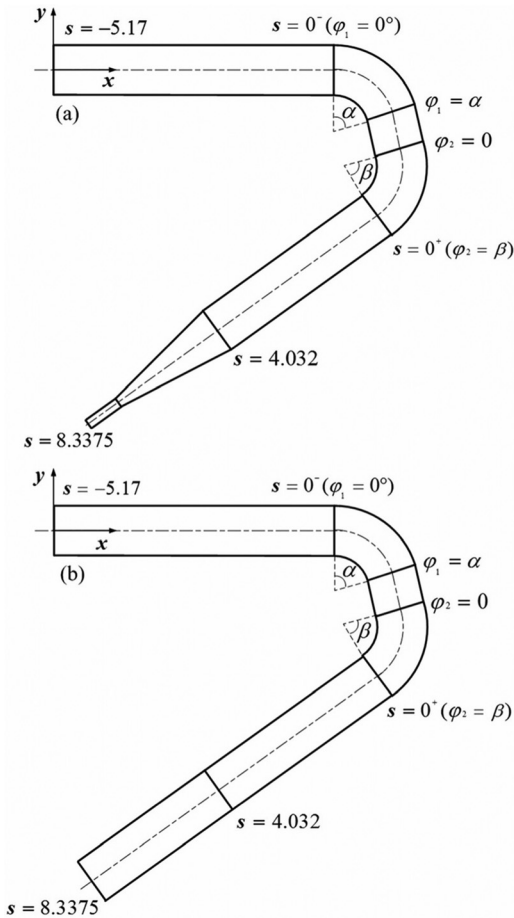
Fig. 2 Coordinates along a curved pipe

The uniqueness of the present study can be found in the effects of the half-bend angle φ (as shown in Fig. 2) and the presence of a nozzle in the exit region of eight pipe configurations on the momentum thickness and turbulence intensity at the pipe exit. The curvature ratios match those of the pipes that are tested in the MERIT experiment. The investigated pipe geometries are shown in Fig. 3.

2 Theoretical Analysis

2.1 Governing Equations. The motion of a fluid particle in a pipe segment, assuming isothermal conditions, is governed by the conservation of mass and momentum in the flow. The cylindrical polar coordinate system (r, θ, z) is used for the baseline straight pipe of the circular cross section, where r is the radial distance, θ is the azimuthal angle, and z is the axial coordinate direction. The vector (u, v, w), in dimensional form, denotes the components of the instantaneous velocity in the r, θ, and z coordinate directions, respectively. Steady state and incompressible flow conditions are assumed. The nondimensional continuity equation in a straight pipe can be written as

$$L_c(u^*, v^*, w^*) = 0 \tag{1}$$

where (u^*, v^*, w^*) are the nondimensional components of the instantaneous velocity.

The nondimensional momentum equations in the normalized r^*, θ^*, and z^* coordinate directions of the straight pipe can be written as

$$L_{M_i}(u^*, v^*, w^*) = 0 \tag{2}$$

where $i = 1$, 2, and 3 refer to the r^*, θ^*, and z^* components, respectively. Thus Ref. [16],

$$L_c(u^*, v^*, w^*) \equiv \frac{\partial u^*}{\partial r^*} + \frac{u^*}{r^*} + \frac{1}{r^*}\frac{\partial v^*}{\partial \theta^*} + \frac{\partial w^*}{\partial z^*} \tag{3}$$

$$L_{M_1}(u^*, v^*, w^*) \equiv u^*\frac{\partial u^*}{\partial r^*} + \frac{v^*}{r^*}\frac{\partial u^*}{\partial \theta^*} + w^*\frac{\partial u^*}{\partial z^*} - \frac{v^{*2}}{r^*} + \frac{\partial p^*}{\partial r^*}$$
$$- \frac{1}{\text{Re}}\left(\nabla^{*2}u^* - \frac{u^*}{r^{*2}} - \frac{2}{r^{*2}}\frac{\partial v^*}{\partial \theta^*}\right) \tag{4}$$

$$L_{M_2}(u^*, v^*, w^*) \equiv u^*\frac{\partial v^*}{\partial r^*} + \frac{v^*}{r^*}\frac{\partial v^*}{\partial \theta^*} + w^*\frac{\partial v^*}{\partial z^*} + \frac{u^* v^*}{r^*} + \frac{1}{r^*}\frac{\partial p^*}{\partial \theta^*}$$
$$- \frac{1}{\text{Re}}\left(\nabla^{*2}v^* + \frac{2}{r^{*2}}\frac{\partial u^*}{\partial \theta^*} - \frac{v^*}{r^{*2}}\right) \tag{5}$$

$$L_{M_3}(u^*, v^*, w^*) \equiv u^*\frac{\partial w^*}{\partial r^*} + \frac{v^*}{r^*}\frac{\partial w^*}{\partial \theta^*} + w^*\frac{\partial w^*}{\partial z^*} + \frac{\partial p^*}{\partial z^*} - \frac{1}{\text{Re}}\nabla^{*2}w^* \tag{6}$$

The scales for nondimensionalization are as follows:

$$u^* = u/U_b, \quad v^* = v/U_b, \quad w^* = w/U_b,$$
$$r^* = r/a, \quad z^* = z/a, \quad p^* = p/\rho U_b^2, \quad \text{Re} \equiv \frac{2aU_b\rho}{\mu} \tag{7}$$

where p is the reduced pressure, ρ is the mass density of fluid, a is the radius of the circular pipe, and U_b is the bulk velocity

$$U_b = \frac{\displaystyle\int u(r, \theta)r\,dr\,d\theta}{\displaystyle\int r\,dr\,d\theta} \tag{8}$$

where $u(r, \theta)$ is the instantaneous axial velocity component. The Laplacian operator ∇^{*2} is

$$\nabla^{*2} \equiv \frac{1}{r^*}\frac{\partial}{\partial r^*}\left(r^*\frac{\partial}{\partial r^*}\right) + \frac{1}{r^{*2}}\frac{\partial^2}{\partial \theta^{*2}} + \frac{\partial^2}{\partial z^{*2}} \tag{9}$$

The motion of a fluid in a curved pipe whose centerline varies locally in a two-dimensional plane will be described in the curvilinear coordinates $(r, \theta, \tilde{z})$, as shown in Fig. 4. The coordinates r and θ are the same as those defined for a straight pipe, while $\tilde{z}$ is a coordinate direction, which is positive along the flow direction and is tangential to the pipe centerline. The coordinates $(r, \theta, \tilde{z})$ are a right-handed system and are always mutually orthogonal when the pipe centerline is a two-dimensional curve [17]. The vector (u, v, w) represents the instantaneous velocity components in the r, θ, and $\tilde{z}$ coordinate directions, respectively.

Murata [17] has analyzed the steady laminar motion of a fluid through pipes of a circular cross section, assuming small centerline curvatures. We use his model as the starting point for identifying the sources of secondary flows and compare the velocity distributions associated with such sources to one obtained from a computational fluid dynamics analysis of the same physical problem. For this purpose, we consider a pipe profile of the form $y = b\sin(nx)$ (see Fig. 4), where $b = 0.1, \ldots, 1, 2, 3, \ldots$ and $n = 0.05, 0.1, \ldots, 1, \ldots$ We illustrate with the results for $b = 3.0$ and $n = 0.1$. The results will be examined at the arbitrary point $x = 60$, where the flow is already fully developed. The following relations are defined
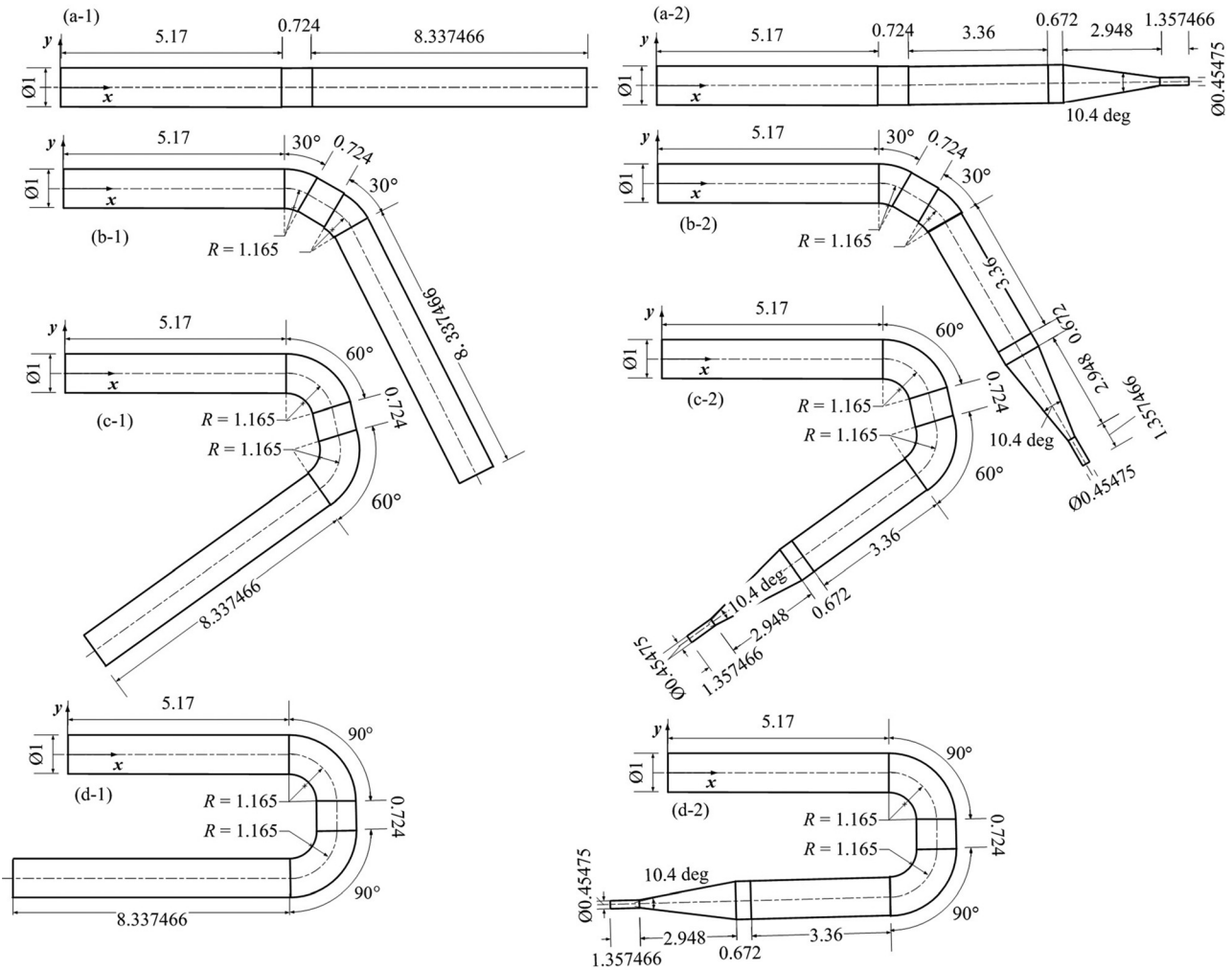
Fig. 3 Configurations of the pipes investigated: without nozzles ($\varphi_1/\varphi_2 =$ (a-1) 0 deg/0 deg, (b-1) 30 deg/30 deg, (c-1) 60 deg/ 60 deg, and (d-1) 90 deg/90 deg); with nozzles ($\varphi_1/\varphi_2 =$ (a-2) 0 deg/0 deg, (b-2) 30 deg/30 deg, (c-3) 60 deg/60 deg, and (d-2) 90 deg/90 deg)

$$x = \tilde{z} - \frac{nbr\cos\theta}{L}\cos(nx), \quad y = b\sin(nx) + \frac{r\cos\theta}{L}, \quad z = r\sin\theta,$$

$$\Gamma^1_{33} = -L\kappa_c\sqrt{g_{33}}\cos\theta, \quad \Gamma^2_{33} = \frac{L}{r}\kappa_c\sqrt{g_{33}}\sin\theta,$$

$$\Gamma^3_{33} = \frac{1}{\sqrt{g_{33}}}\frac{\partial}{\partial\tilde{z}}\sqrt{g_{33}}, \quad \Gamma^3_{23} = \Gamma^3_{32} = -\frac{L}{\sqrt{g_{33}}}\kappa_c r\sin\theta,$$

$$\Gamma^3_{13} = \Gamma^3_{31} = \frac{L}{\sqrt{g_{33}}}\kappa_c\cos\theta \tag{10}$$

where

$$L = [1 + n^2 b^2 \cos^2(nx)]^{1/2} \tag{11}$$

$$\sqrt{g_{33}} = L(1 + r\kappa_c\cos\theta) \tag{12}$$

$$\kappa_c = \frac{n^2 b\sin(nx)}{L^3} \tag{13}$$

Compared to Eqs. (4) through (6), the additional terms can be nondimensionalized using the following scales:

$$g^*_{33} = g_{33}, \quad \Gamma^{1*}_{33} = a\Gamma^1_{33}, \quad \Gamma^{2*}_{33} = \Gamma^2_{33}a^2, \quad \Gamma^{3*}_{13} = a\Gamma^3_{13},$$
$$\Gamma^{3*}_{31} = a\Gamma^3_{31}, \quad \Gamma^{3*}_{23} = \Gamma^3_{23}, \quad \Gamma^{3*}_{32} = \Gamma^3_{32}, \quad \Gamma^{3*}_{33} = a\Gamma^3_{33} \tag{14}$$

The nondimensional continuity and momentum equations can then be written as follows:
Continuity

$$\tilde{L}_c(u^*, v^*, w^*) = 0 \tag{15}$$

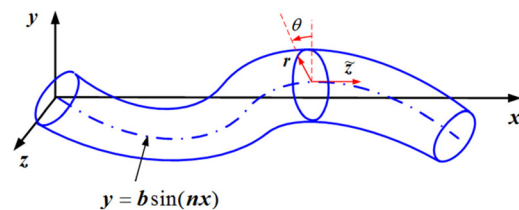where

$$\tilde{L}_c(u^*, v^*, w^*) = \frac{1}{r^*}\frac{\partial(r^* u^*)}{\partial r^*} + \frac{1}{r^*}\frac{\partial v^*}{\partial\theta} + \frac{1}{\sqrt{g_{33}}}\frac{\partial w^*}{\partial\tilde{z}^*}$$
$$+ \Gamma^{3*}_{31}u^* + \Gamma^{3*}_{32}\frac{v^*}{r^*} \tag{16}$$

Momentum

$$\tilde{L}_{M_i}(u^*, v^*, w^*) = 0 \tag{17}$$

Fig. 4 Curvilinear coordinates for the periodically-curved pipe

where

$$\tilde{L}_{M_1}(u,v,w) = u^* \frac{\partial u^*}{\partial r^*} + \frac{v^*}{r^*}\frac{\partial u^*}{\partial \theta^*} - \frac{v^{*2}}{r^*} + \frac{w^*}{\sqrt{g_{33}}}\frac{\partial u^*}{\partial \tilde{z}^*} + \Gamma_{33}^{1*}\frac{w^{*2}}{g_{33}} + \frac{\partial p^*}{\partial r^*} - \frac{1}{\mathrm{Re}}\left[\frac{\partial^2 u^*}{\partial r^{*2}} + \frac{1}{r^*}\frac{\partial u^*}{\partial r^*} - \frac{u^*}{r^{*2}} + \frac{1}{r^{*2}}\frac{\partial^2 u^*}{\partial \theta^{*2}} + \frac{1}{g_{33}}\frac{\partial^2 u^*}{\partial \tilde{z}^{*2}} - \frac{2}{r^{*2}}\frac{\partial v^*}{\partial \theta^*}\right.$$
$$\left. + \frac{\Gamma_{33}^{1*}}{g_{33}}\left(\Gamma_{13}^{3*}u^* + \Gamma_{23}^{3*}\frac{v^*}{r^*} - \frac{\partial u^*}{\partial r^*}\right) + \frac{\Gamma_{33}^{3*}}{g_{33}}\frac{\partial u^*}{\partial \tilde{z}^*} + \frac{1}{g_{33}}\left\{\frac{w^*}{\sqrt{g_{33}}}\frac{\partial}{\partial \tilde{z}^*}(\Gamma_{33}^{1*}) + 2\Gamma_{33}^{1*}\frac{\partial}{\partial \tilde{z}^*}\left(\frac{w^*}{\sqrt{g_{33}}}\right)\right\}\right] \tag{18}$$

$$\tilde{L}_{M_2}(u^*,v^*,w^*) = u^* \frac{\partial v^*}{\partial r^*} + \frac{v^*}{r^*}\frac{\partial v^*}{\partial \theta*} + \frac{u^* v^*}{r^*} + \frac{w^*}{\sqrt{g_{33}}}\frac{\partial v^*}{\partial \tilde{z}^*} + \Gamma_{33}^{2*}\frac{r^* w^{*2}}{g_{33}} + \frac{1}{r^*}\frac{\partial p^*}{\partial \theta^*} - \frac{1}{\mathrm{Re}}\left[\frac{\partial^2 v^*}{\partial r^{*2}} + \frac{1}{r^*}\frac{\partial v^*}{\partial r^*} - \frac{v^*}{r^{*2}} + \frac{1}{r^{*2}}\frac{\partial^2 v^*}{\partial \theta^{*2}} + \frac{1}{g_{33}}\frac{\partial^2 v^*}{\partial \tilde{z}^{*2}} + \frac{2}{r^{*2}}\frac{\partial u^*}{\partial \theta^*}\right.$$
$$\left. - \frac{\Gamma_{33}^{1*}}{g_{33}}\frac{\partial v^*}{\partial r^*} + \frac{\Gamma_{33}^{2*}}{g_{33}}\left(\Gamma_{13}^{3*}r^*u^* - u^* + \Gamma_{23}^{3*}v^* - \frac{\partial v^*}{\partial \theta^*}\right) - \frac{\Gamma_{33}^{3*}}{g_{33}}\frac{\partial v^*}{\partial \tilde{z}^*} + \frac{r^*}{g_{33}}\left\{\frac{w^*}{\sqrt{g_{33}}}\frac{\partial}{\partial \tilde{z}^*}(\Gamma_{33}^{2*}) + 2\Gamma_{33}^{2*}\frac{\partial}{\partial \tilde{z}^*}\left(\frac{w^*}{\sqrt{g_{33}}}\right)\right\}\right] \tag{19}$$

$$\tilde{L}_{M_3}(u^*,v^*,w^*) = u^* \frac{\partial^*}{\partial r^*}\left(\frac{w^*}{\sqrt{g_{33}}}\right) + \frac{v^*}{r^*}\frac{\partial}{\partial \theta*}\left(\frac{w^*}{\sqrt{g_{33}}}\right) + \frac{w^*}{g_{33}}\frac{\partial w^*}{\partial \tilde{z}^*} + \frac{2w^*}{\sqrt{g_{33}}}\left(\Gamma_{31}^{3*}u^* + \Gamma_{32}^{3*}\frac{v^*}{r^*}\right) + \frac{1}{g_{33}}\frac{\partial p^*}{\partial \tilde{z}^*}$$
$$- \frac{1}{\mathrm{Re}}\left[\frac{\partial^2}{\partial r^{*2}}\left(\frac{w^*}{\sqrt{g_{33}}}\right) + \frac{1}{r^*}\frac{\partial}{\partial r^*}\left(\frac{w^*}{\sqrt{g_{33}}}\right) + \frac{1}{r^{*2}}\frac{\partial^2}{\partial \theta^2}\left(\frac{w^*}{\sqrt{g_{33}}}\right) + \frac{1}{g_{33}}\frac{\partial}{\partial \tilde{z}^*}\left(\frac{1}{\sqrt{g_{33}}}\frac{\partial w^*}{\partial \tilde{z}^*}\right)\right.$$
$$+ \frac{1}{g_{33}}\left\{u^*\frac{\partial}{\partial \tilde{z}^*}(\Gamma_{13}^{3*}) + \frac{v^*}{r^*}\frac{\partial}{\partial \tilde{z}^*}(\Gamma_{23}^{3*})\right\} + \frac{w^*}{\sqrt{g_{33}}}\left\{\frac{\partial}{\partial r^*}(\Gamma_{13}^{3*}) + \frac{1}{r^{*2}} + \frac{\partial}{\partial \theta}(\Gamma_{23}^{3*})\right\}$$
$$+ \Gamma_{13}^{3*}\left\{\frac{2}{g_{33}}\frac{\partial u^*}{\partial \tilde{z}^*} + 2\frac{\partial}{\partial r^*}\left(\frac{w^*}{\sqrt{g_{33}}}\right) + \frac{1}{r^*}\frac{w^*}{\sqrt{g_{33}}}\right\} + \frac{2\Gamma_{23}^{3*}}{r^{*2}}\left\{\frac{r}{g_{33}}\frac{\partial v^*}{\partial \tilde{z}^*} + \frac{\partial}{\partial \theta*}\left(\frac{w^*}{\sqrt{g_{33}}}\right)\right\}$$
$$\left. + \frac{w^*}{\sqrt{g_{33}}}\left\{(\Gamma_{13}^{3*})^2 + \left(\frac{\Gamma_{32}^{3*}}{r^*}\right)^2\right\} - \frac{1}{g_{33}}\left\{\Gamma_{33}^{3*}\frac{\partial}{\partial r^*}\left(\frac{w^*}{\sqrt{g_{33}}}\right) + (\Gamma_{33}^{2*}\frac{\partial}{\partial \theta*}\left(\frac{w^*}{\sqrt{g_{33}}}\right))\right\}\right] \tag{20}$$

2.2 Understanding the Secondary Flows.

To better understand the secondary flows in a curved pipe, we compare the governing equations for a curved pipe with those for a straight pipe and study the terms that represent the differences between two sets of equations. We decompose the equations for a curved pipe as follows:

$$\tilde{L}_c(u^*,v^*,w^*) = L_c(u^*,v^*,w^*) + D_c^* \tag{21}$$

$$\tilde{L}_{M_1}(u^*,v^*,w^*) = L_{M_1}(u^*,v^*,w^*) + D_r^* \tag{22}$$

$$\tilde{L}_{M_2}(u^*,v^*,w^*) = L_{M_2}(u^*,v^*,w^*) + D_\theta^* \tag{23}$$

$$\tilde{L}_{M_3}(u^*,v^*,w^*) = L_{M_3}(u^*,v^*,w^*) + D_{\tilde{z}}^* \tag{24}$$

where the first terms on the right-hand side of the equations represent the contribution of a straight pipe and the remaining terms are due to the curvature. For fully-developed laminar flow in a straight pipe $D_c^* = D_r^* = D_\theta^* = D_{\tilde{z}}^* = 0$, $g_{33} = 0$, $\kappa_c = 0$, $L = 0$, $\Gamma_{ij}^{k*} = 0$, $u^* = v^* = 0$, and $w^* = w^*(r^*)$. For fully-developed laminar flow in the sinusoidal pipe configuration ($y = b\sin(nx)$), Eqs. (10) to (13) and the conditions $u^* = u^*(r^*,\theta^*)$, $v^* = v^*(r^*,\theta^*)$, and $w^* = w^*(r^*,\theta^*)$ lead to the following simplification of the curvature terms:

$$D_c^*(u^*,v^*,w^*) \equiv \Gamma_{31}^{3*}u^* + \Gamma_{32}^{3*}\frac{v^*}{r^*} = \frac{\kappa_c\cos\theta^*}{1 + r^*\kappa_c\cos\theta^*}u^*$$
$$- \frac{\kappa_c\sin\theta^*}{1 + r^*\kappa_c\cos\theta^*}v^* \tag{25}$$

$$D_r^*(u^*,v^*,w^*) \equiv \Gamma_{33}^{1*}\frac{w^{*2}}{g_{33}} = -\frac{w^{*2}\kappa_c\cos\theta^*}{1 + r^*\kappa_c\cos\theta^*} \tag{26}$$

$$D_\theta^*(u^*,v^*,w^*) \equiv \Gamma_{33}^{2*}\frac{r^* w^{*2}}{g_{33}} = \frac{w^{*2}\kappa_c\sin\theta^*}{1 + r^*\kappa_c\cos\theta^*} \tag{27}$$

$$D_{\tilde{z}}^*(u^*,v^*,w^*) \equiv \left(u^*\frac{\partial w^*}{\partial r^*} + \frac{v^*}{r^*}\frac{\partial w^*}{\partial \theta^*}\right)\left(\frac{1}{\sqrt{g_{33}}} - 1\right)$$
$$- \frac{w^*}{g_{33}}\left(u^*\frac{\partial \sqrt{g_{33}}}{\partial r^*} - \frac{v^*}{r^*}\frac{\partial \sqrt{g_{33}}}{\partial \theta^*}\right)$$
$$+ \frac{\partial p^*}{\partial \tilde{z}^*}\left(\frac{1}{g_{33}} - 1\right) + \frac{2w^*}{\sqrt{g_{33}}}\left(\Gamma_{31}^{3*}u^* + \Gamma_{32}^{3*}\frac{v^*}{r^*}\right)$$
$$= \left(u^*\frac{\partial w^*}{\partial r^*} + \frac{v^*}{r^*}\frac{\partial w^*}{\partial \theta^*}\right)\left[\frac{1}{L(1 + r\kappa_c\cos\theta^*)} - 1\right]$$
$$- \frac{w^*}{g_{33}}\left(u^*\frac{\partial \sqrt{g_{33}}}{\partial r^*} - \frac{v^*}{r^*}\frac{\partial \sqrt{g_{33}}}{\partial \theta^*}\right)$$
$$+ \frac{\partial p^*}{\partial \tilde{z}^*}\left(\frac{1}{L^2(1 + r\kappa_c\cos\theta^*)^2} - 1\right)$$
$$+ \frac{2w^*}{\sqrt{g_{33}}}\kappa_c\frac{\cos\theta^*u^* - \sin\theta^*v^*}{1 + r^*\kappa_c\cos\theta^*} \tag{28}$$

We propose that Eqs. (26) and (27) describe the secondary flows in a curved pipe. To test this hypothesis, we evaluate these terms (D_r^* and D_θ^*) using velocities obtained from a straight pipe and compare the results to the velocities (u^* and v^*) obtained directly from a numerical simulation of the flow in the curved pipe. Physically, D_r^* and D_θ^* represent inertial forces due to the presence of the curvature, with units in Newton's when expressed in dimensional form. The profiles of u^* and v^* are plotted in Figs. 5(a) and 5(b), respectively.

The iso-contours of D_r^* and D_θ^* are obtained by substituting the straight-pipe velocity solutions into the expressions for these terms. The results are shown in Figs. 5(c) and 5(d). The qualitative similarity between Figs. 5(a) (Figs. 5(b)) and 5(c) (Fig. 5(d)) support the suggestion that the previously identified inertial terms determine the secondary flow in curved pipes. The inertial terms identified in this paper are consistent with the centrifugal force terms discussed in Berger et al. [18]. It is also important to note that D_r^* and D_θ^* do not include the terms v^{*2}/r^* and u^*v^*/r^*,
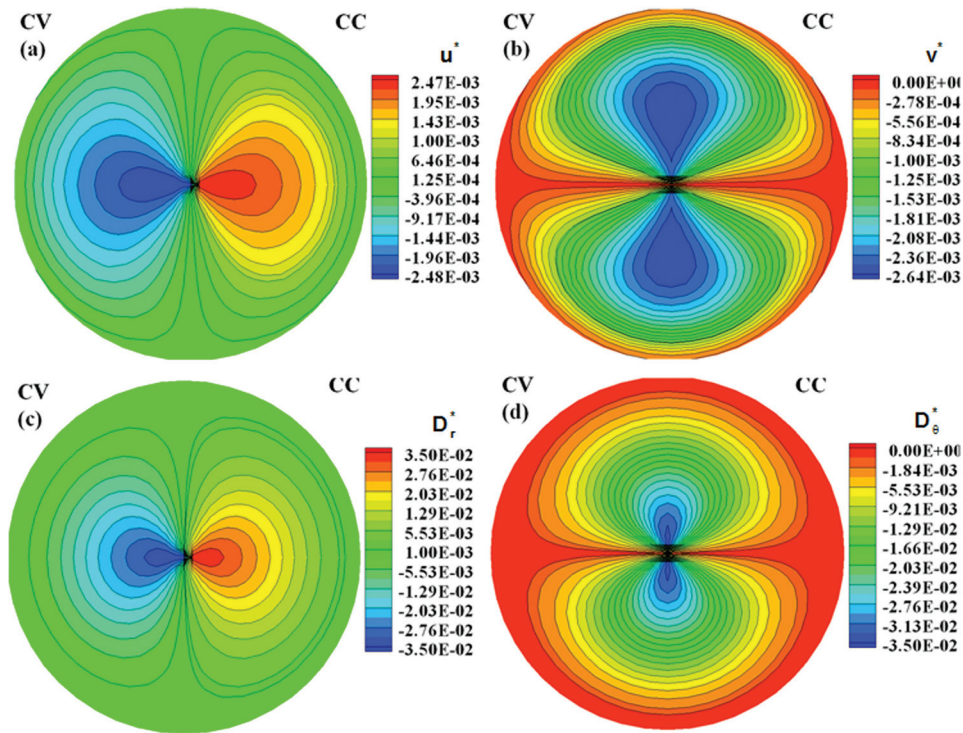
Fig. 5 Contour plots of (*a*) u^*, and (*b*) v^* at $x = 60$ of the periodically-curved pipe (Re = 1000) and contour plots of (*c*) D_r^*, and (*d*) D_θ^* based on the straight pipe velocity field. Here, CV implies "convex (inner) side," CC is the "concave (outer) side."

respectively. Although these other terms were referred to as centrifugal force terms by Webster and Humphrey [19], it seems as if the significance of these terms is found in their ability to promote instability, even in a straight pipe.

The authors acknowledge that the procedure just described for identifying the secondary flow terms in the equations is *ad hoc*. A more rigorous approach could try to isolate explicit physically-meaningful terms in the momentum equations in the same manner that the Navier–Stokes equations in a rotating frame of reference introduce the additional terms $\rho[\omega \times \omega \times \mathbf{r} + 2\omega \times \mathbf{u}]$ [20], which, respectively, consist of the centrifugal and Coriolis force fields. (Here, ω, $\mathbf{r}$, and $\mathbf{u}$ are the vectors of the angular velocity, position, and instantaneous rotating frame velocity, respectively.) The present problem appears to be more complicated and the foregoing analysis has been undertaken only for the insight.

3 Numerical Simulations

A RANS equation approach will suffice for the current problem in which the fluid is bounded by a circular no-slip wall and the interest is mainly on the mean flow. The Reynolds stress model (RSM) [21] has been judged to be the most accurate RANS model for turbulent flow in curved pipes, since it includes memory effects and the effects of streamline curvature. However, the RSM is a six-equation model that is computationally expensive for practical engineering problems. Several options exist for the simpler one- or two-equation RANS approaches, including the Spalart–Allmaras (SA), [22] standard $k - \varepsilon$ (SKE) [23], and realizable $k - \varepsilon$ (RKE) [24] models. A curved-pipe flow problem is simulated with these methods for the purpose of down selection.

The test conditions are taken from Sudo [12] and consist of a 90 deg bend with $\delta = 1/4$ (see Fig. 6). The pipe has a 100-diameter upstream tangent section and a 40-diameter downstream tangent section. The results are compared in Fig. 7 for the static pressure coefficient C_p at 17.6 diameters upstream of the bend.

The variable s is a pseudo coordinate direction, which is introduced in this section for the purpose of describing the locations on the straight (tangent) portions of the pipe. In Sudo's measurements, the upstream tangent is $-1 \leq s \leq 0^-$ and the region after the bend is $0^+ \leq s \leq 5$. Note that $\theta = -90$ deg is the convex side of the bend, while $\theta = 90$ deg is the concave side, which is consistent with the use in Sudo's experiment. Fairly close agreement between the methods is apparent. However, the RKE results
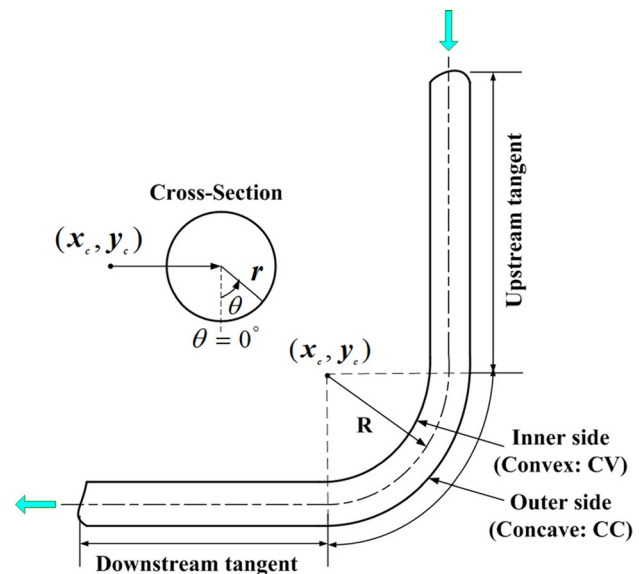
Fig. 6 The sketch of a curved pipe with a 90 deg bend. Here, CV implies "convex (inner) side," CC is the "concave (outer) side," (x_c, y_c) denotes the curvature center, and R is the radius of curvature.
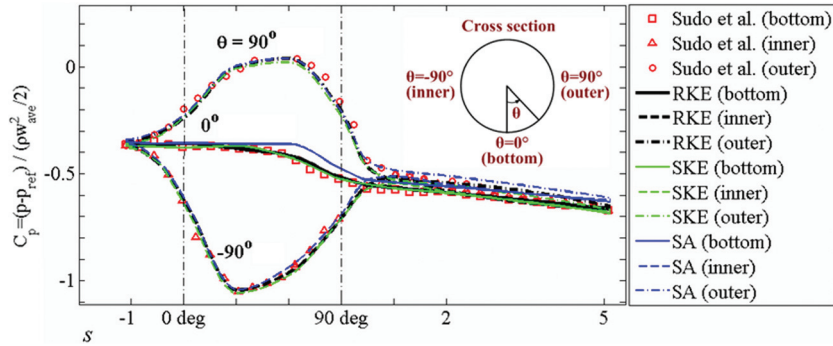
Fig. 7 Longitudinal distribution of static pressure at the convex ($\theta = -90$ deg), concave ($\theta = 90$ deg), and bottom ($\theta = 0$ deg) regions of the 90 deg bend (Re = 60,000)

match the experimental data better than the results from the SA and SKE models for the three locations plotted in Fig. 7. Thus, the RKE model has been selected for use in subsequent pipe calculations in this paper.

Since mercury flow becomes fully-developed long before approaching the first 90 deg half-bend angle, this geometry has been simplified by shortening the inflow section. The eight geometries investigated (see Fig. 3) have length dimensions that are the same as in the MERIT experiment: the pipe radius is a, the curvature radius $R = 2.33a$, and the inflow and outflow lengths of the straight pipe are matched, with and without a nozzle at the exit region. The investigated half-bend angles φ_1/φ_2 are 0 deg /0 deg, 30 deg /30 deg, 60 deg /60 deg, and 90 deg /90 deg. The Reynolds number, based on the bulk velocity and pipe diameter, is approximately equal to 8.244×10^5 at the inlet but the value in the vicinity of the exit in tapered tubes is approximately 1.813×10^6. The Dean number is 5.401×10^5.

The computational grid points are $3.7 \times 10^6 \sim 5 \times 10^6$ and $3.9 \times 10^6 \sim 5.8 \times 10^6$ for pipes of various half-bend angles without and with nozzles, respectively. The first mesh size in the r direction uses 5.56×10^{-5} pipe diameters, which corresponds to a y^+ of approximately 0.94. Note that approximately 30 grid points are located within $y^+ < 30$. We use 48 grid points in the circumferential direction and the grid density is 1.8 deg /node in the vicinity of the bend.

4 Results and Discussion

The three-dimensional incompressible RANS are solved to predict the turbulent flow of mercury inside the pipes. The mean flow ($\mathbf{U}^*, P^*$) is related to the total or instantaneous ($\mathbf{u}^*, p^*$) and fluctuating (($\mathbf{u}'$)*, (p')*) components as follows:

$$\mathbf{u}^* = \mathbf{U}^* + (\mathbf{u}')^* \tag{29}$$

$$p^* = P^* + (p')^* \tag{30}$$

The governing equations for the mean flow can be expressed in terms of mass conservation (continuity)

$$\nabla^* \cdot \mathbf{U}^* = 0 \tag{31}$$

and momentum conservation

$$\mathbf{U}^* \cdot \nabla^* \mathbf{U}^* = -\frac{1}{\rho^*} \nabla^* P^* + \frac{1}{\mathrm{Re}} \nabla^* \cdot \tau^* \tag{32}$$

The shear stress tensor τ^* is modeled as

$$\tau^*_{ij} = (\nu^* + \nu^*_t)\left(\frac{\partial U^*_i}{\partial x^*_j} + \frac{\partial U^*_j}{\partial x^*_i}\right) \tag{33}$$

and the eddy viscosity is computed from

$$\nu^*_t = C_\mu \frac{k^{*2}}{\varepsilon^*} \tag{34}$$

where k^* is the kinetic energy of turbulence, $k^* \equiv (1/2)(\overline{(u')^{*2}} + \overline{(v')^{*2}} + \overline{(w')^{*2}})$, and ε^* is its dissipation rate. Here, C_μ is modeled as [24]

$$C_\mu = \frac{1}{A_0 + A_s \dfrac{k^* U^{(*)}}{\varepsilon^*}} \tag{35}$$

where

$$U^{(*)} \equiv \sqrt{S^*_{ij} S^*_{ij} + \overline{\Omega}^*_{ij} \overline{\Omega}^*_{ij}} \tag{36}$$

$$S^*_{ij} = \frac{1}{2}(U^*_{i,j} + U^*_{j,i}) \tag{37}$$

$$\overline{\Omega}^*_{ij} = \frac{1}{2}(U^*_{i,j} - U^*_{j,i}) \tag{38}$$

where S^*_{ij} is the symmetric part of the velocity gradient tensor, with $\overline{\Omega}^*_{ij}$ the antisymmetric part. The model constants A_0 and A_s are given as [24]

$$A_0 = 4.04, \quad A_s = \sqrt{6}\cos\phi \tag{39}$$

where

$$\phi = \frac{1}{3}\cos^{-1}(\sqrt{6}W), \quad W = \frac{S^*_{ij}S^*_{jk}S^*_{ki}}{\tilde{S}^{*3}}, \quad \tilde{S}^* = \sqrt{S^*_{ij}S^*_{ij}} \tag{40}$$

The nondimensional equations for k^* and ε^* can then be written as [24]

$$\mathbf{U}^* \cdot \nabla^* k^* = \nabla^*\left[\left(\frac{1}{\mathrm{Re}} + \frac{1}{\sigma_k \mathrm{Re}_t}\right)\nabla^* k^*\right] + G^*_t - \varepsilon^* \tag{41}$$

$$\mathbf{U}^* \cdot \nabla^* \varepsilon^* = \nabla^*\left[\left(\frac{1}{\mathrm{Re}} + \frac{1}{\sigma_\varepsilon \mathrm{Re}_t}\right)\nabla^* \varepsilon^*\right]$$
$$+ C_1 S^* \varepsilon^* - C_2 \frac{1}{a}\frac{\varepsilon^{*2}}{k^* + \sqrt{\nu^* \varepsilon^*}} \tag{42}$$

where σ_k and σ_ε are the turbulent Prandtl numbers for k^* and ε^*, respectively. Here, Re_t is the Reynolds number based on the eddy viscosity (see Eq. (34)).

Table 1 The constants for the RKE model

σ_k	σ_ε	C_1	C_2	Re_t
1.0	1.2	$\max\left[0.43, \dfrac{\eta}{\eta+5}\right]$ [a]	1.9	$0.185727\dfrac{\varepsilon}{C_\mu k^{*2}}$

[a]Note that $\eta = S^* k^*/\varepsilon^*$ and $S^* = \sqrt{2\tilde{S}^*}$.

The production of turbulence kinetic energy G_t^* is evaluated in a manner consistent with the Boussinesq hypothesis

$$G_t^* = \left(2\frac{1}{Re_t}S_{ij}^* - \frac{2}{3}k^*\delta_{ij}\right)U_{i,j}^* \qquad (43)$$

The coefficients in Eqs. (41) and (42) are shown in the Table 1. The inlet velocity for all pipes is that of a fully developed flow in a straight pipe aligned with the z-direction

$$U^* = V^* = 0, \quad W^* = W^*(r^*) \qquad (44)$$

The discrete form of $W^*(r^*)$ is taken as the solution at the exit of a straight pipe obtained from an auxiliary simulation with the axial velocity profile shown in Fig. 8. At the inlet, the mean pressure is $P = 30$ bar, while the turbulence conditions are

$$k^* = \frac{3}{2}(U^*I)^2, \quad \varepsilon^* = \frac{C_\mu^{3/4}k^{*\,3/2}}{l^*} \qquad (45)$$

where I is the turbulence intensity $I = 0.16Re^{-1/8}$. Note that this expression for I is consistent with the definition used for this variable later in the paper (see Eq. (49)). However, the value of k^* at the inlet (see Eq. (45)) is not explicitly known to the authors from the source of the inlet data, although it has presumably been
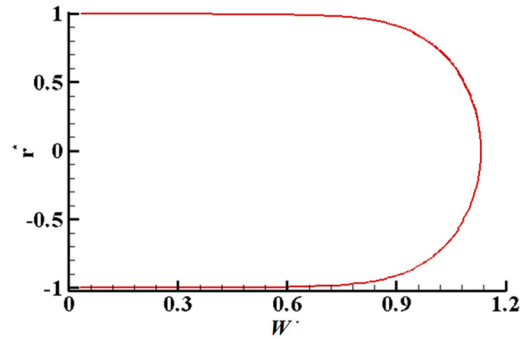
Fig. 8 Fully developed normalized velocity profile at the pipe inlet

factored into the expression for the inlet value of I. The values of C_μ and l^* are

$$C_\mu = 0.09, \quad l^* = 0.07D_h^* \qquad (46)$$

and $D_h^* = 2$. The no-slip conditions are specified at the wall

$$U^* = V^* = W^* = 0 \qquad (47)$$

while zero-gradient conditions are assumed at the pipe exit

$$\nabla_n^* U^* = \nabla_n^* V^* = \nabla_n^* W^* = \nabla_n^* P^* = \cdots = 0 \qquad (48)$$

where $\nabla_n^* \equiv \partial^*/\partial n^*$ and "n^*" is the outward-pointing normal at the outlet.

One goal of the present study is to determine the pipe configuration that has the potential to give the least disturbance in the circular jet shear layer that eventually issues from the nozzle.
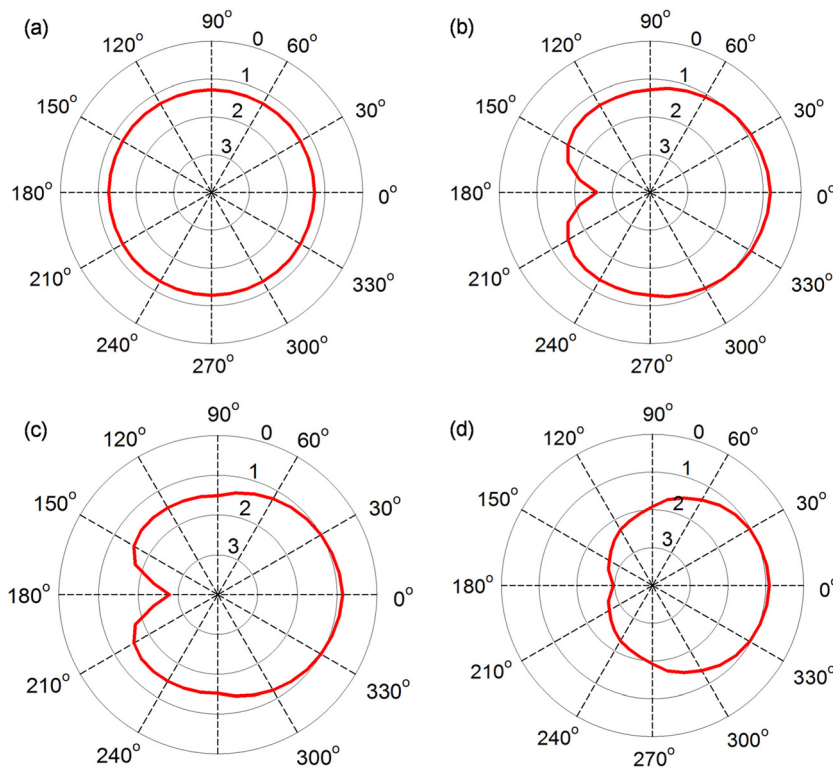
Fig. 9 Momentum thickness distribution at the exit plane of the pipes with half-bend angles of: (a) 0 deg/0 deg, (b) 30 deg/30 deg, (c) 60 deg/60 deg, and (d) 90 deg/90 deg. These pipes have nozzles and $\theta = 180$ deg, 0 deg correspond to the convex and concave sides of the pipes, respectively.
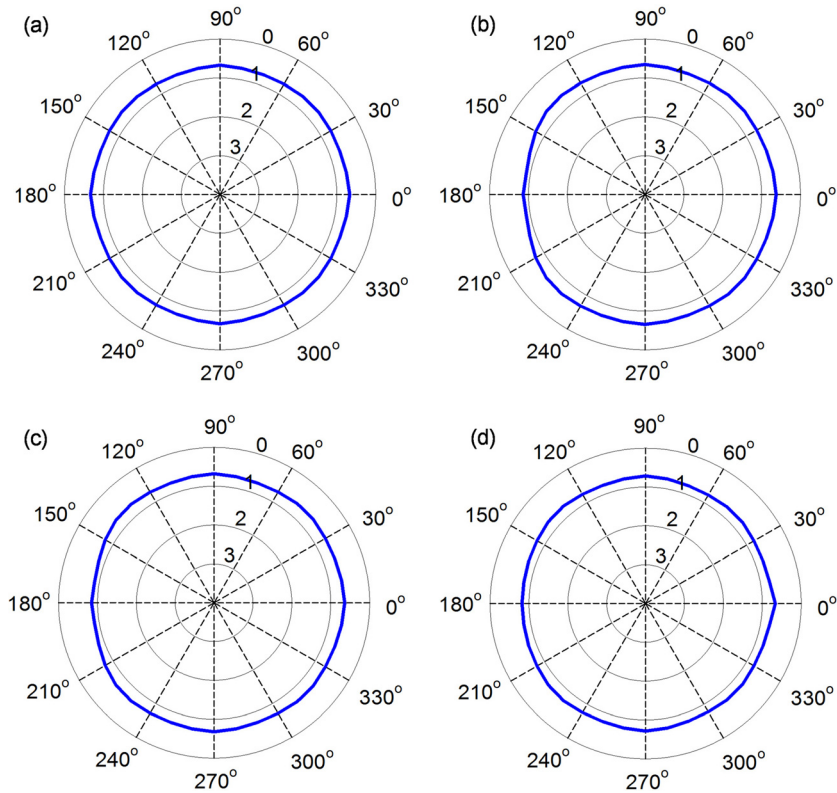
Fig. 10 Momentum thickness distribution at the exit plane of the pipes with half-bend angles of: (a) 0 deg/0 deg, (b) 30 deg/30 deg, (c) 60 deg/60 deg, and (d) 90 deg/90 deg. These pipes have nozzles and $\theta = 180$ deg, 0 deg correspond to the convex and concave sides of the pipes, respectively.

Therefore, some knowledge of the distribution of the momentum thickness δ_θ at the nozzle exit becomes important. For example, the linear stability analysis of Michalke [25] and Plaschko [26] and the experimental work of Cohen and Wygnanski [27], Corke et al. [28], and Corke and Kusek [29] showed that for $2a/\delta_\theta \gg 1$, both the axisymmetric ($m = 0$) and the first spinning or helical instability modes ($m = \pm 1$) are unstable in the initial jet shear layer.

4.1 Momentum Thickness. The polar distribution of δ_θ is shown in Figs. 9 and 10 for pipes without and with nozzles, respectively. The number "0" in the polar plots refers to the wall, while the numbers "1," "2," and "3," respectively, refer to the distances 0.1a, 0.2a, and 0.3a measured from the wall. The momentum thickness decreases with decreasing radius. For pipes without nozzles (see Fig. 9), the distribution of δ_θ is nonuniform at the exit but appears to be similar for the different pipes. The azimuthal variation of δ_θ becomes stronger as the half-bend angle increases. Thus, the 90 deg /90 deg shows the strongest azimuthal variation of δ_θ compared to other pipes. At the exit plane, δ_θ attains its minimum value at $\theta = 0$ deg and its maximum value at $\theta = 180$ deg. Note that the straight pipe does not show an azimuthal variation of δ_θ. Figure 10 shows a fairly uniform δ_θ distribution for all pipes when nozzles are present at the exit.

The differences in the azimuthal variation of δ_θ can be explained by the relationship between the momentum thickness and axial velocity, where the latter, at the pipe exit, is shown in Figs. 12 through 15 for the various pipe configurations. Note that the 90 deg /90 deg pipe shows the most asymmetry in the distribution of the axial velocity (see Fig. 15) and, hence, in the azimuthal distribution of δ_θ. For pipes with nozzles, the axial velocity is fairly uniform in the azimuth, which explains the uniform azimuthal distribution of δ_θ.

4.2 Turbulence Intensity. The turbulence intensity at the exit of the pipes is of interest, as it arguably determines the turbulence level in the jet (not shown). This quantity is defined in this paper as

$$I = \sqrt{\frac{2}{3}\left(\frac{k^*}{U_b^{*2}}\right)} \qquad (49)$$

where k^* is the turbulence kinetic energy per unit mass and U_b^* has been used as a reference for defining the turbulence intensity. The radial distribution of I at the exit plane along the horizontal direction is presented in Fig. 11. Here, I is found to have high values near the walls, with a large gradient for all pipes. We observe that I is significantly reduced when a nozzle is present. For the pipe without a nozzle, I increases as the half-bend angle increases. For example, the 90 deg /90 deg pipe has the strongest turbulence intensity. The radial distribution of I is symmetric for the straight pipe (0 deg /0 deg) with a flat interior, as expected. The profile of I with r^* along the horizontal direction for the 30 deg /30 deg, 60 deg /60 deg, and 90 deg /90 deg pipes without nozzles shows higher values near $r^* = -1$ (the inner side) compared to $r^* = 1$ (the outer side). The higher values of I on the inner side for the pipe without a nozzle are related to the instabilities associated with an adverse pressure gradient. With nozzles, there is a steeper radial gradient of I near wall in the 0 deg /0 deg, 30 deg /30 deg, 60 deg /60 deg, and 90 deg /90 deg pipes compared to those without nozzles. Here, I is nearly flat in the interior region ($-0.6 < r^* < 0.6$). In the region of $-1 < r^* < -0.6$, I has relatively higher values when the half-bend angle is 30 deg compared to other cases. Generally speaking, the straight pipe with a nozzle shows the least turbulence intensity among all eight pipes.
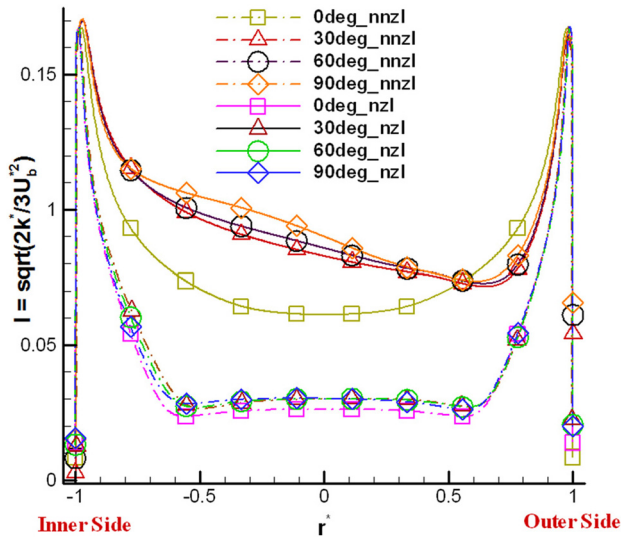
Fig. 11 The horizontal distribution of the turbulence intensity at the exit plane. The subscripts "nzl" and "nnzl" denote the presence or absence of a nozzle at the pipe exit.
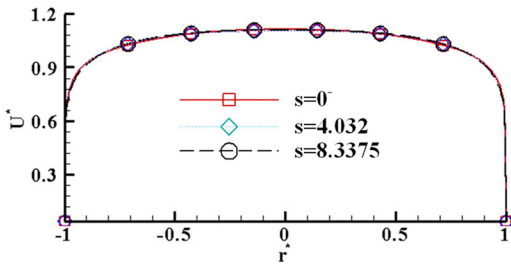

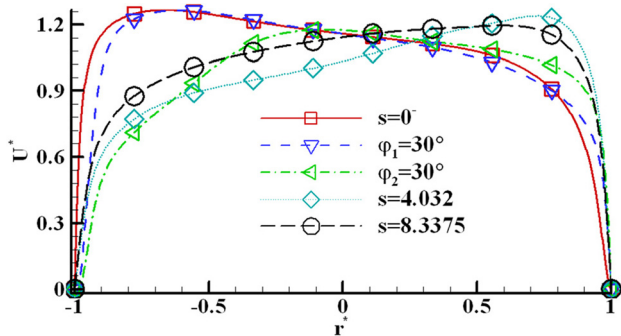**Fig. 12 Radial distribution of the U^* in the 0 deg/0 deg pipe**

Fig. 13 Radial distribution of U^* in the 30 deg/30 deg pipe

Fig. 14 Radial distribution of U^* in the 60 deg/60 deg pipe

Fig. 15 Radial distribution of U^* in the 90 deg/90 deg pipe

Fig. 16 Radial distribution of U^* in the 0 deg/0 deg pipe without (squares) and with (triangles) a nozzle at the following 3 locations along the pipe: (a) $s = 0^-$, (b) $s = 4.032$, and (c) $s = 8.3375$

4.3 Axial Velocity Distribution. As stated earlier, the pseudo coordinate distance s is used to describe the locations of points in the straight portions of the pipe, while the bend angles φ_1 and φ_2 are used for the curved portions. These coordinates are depicted in Fig. 2. The upstream tangents of all of the curved pipes investigated in this paper are of the same length ($-5.17 \leq s \leq 0^-$); so are the downstream tangents ($0^+ \leq s \leq 8.3375$). Figures 12 through 15 show the radial (r^*) axial-velocity (U^*) distribution for pipes without a nozzle. Note that the effects of the bend angle on the flow in the curved pipes are presented only for the cases without nozzles.

In Fig. 12, the velocity distribution is identical for the three values of distance s examined, since there is no bend and the flow has already reached the fully developed profile at the inlet of the
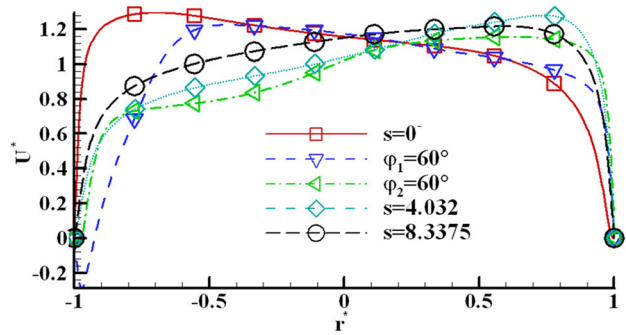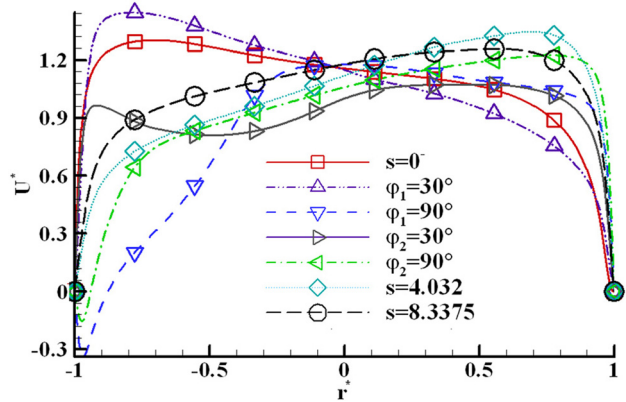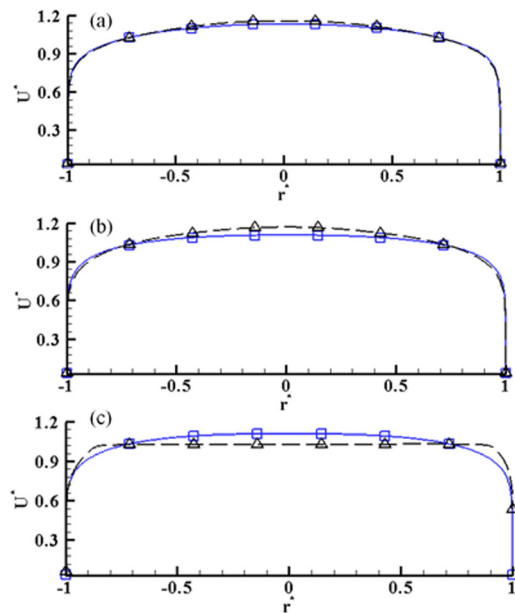
pipe. However, for the curved pipes and when $s = 0^-$, the convex (inner) side of the pipe (near $r^* = -1$) shows higher magnitudes of U^* compared to the concave (outer) side of the pipe. This is also the case at the end of the first bend for the 30 deg/30 deg and 60 deg/60 deg pipes. Note that $\varphi_1 = 30$ deg (see Fig. 13) and 60 deg (see Fig. 14), respectively, for this location in the two

Journal of Fluids Engineering
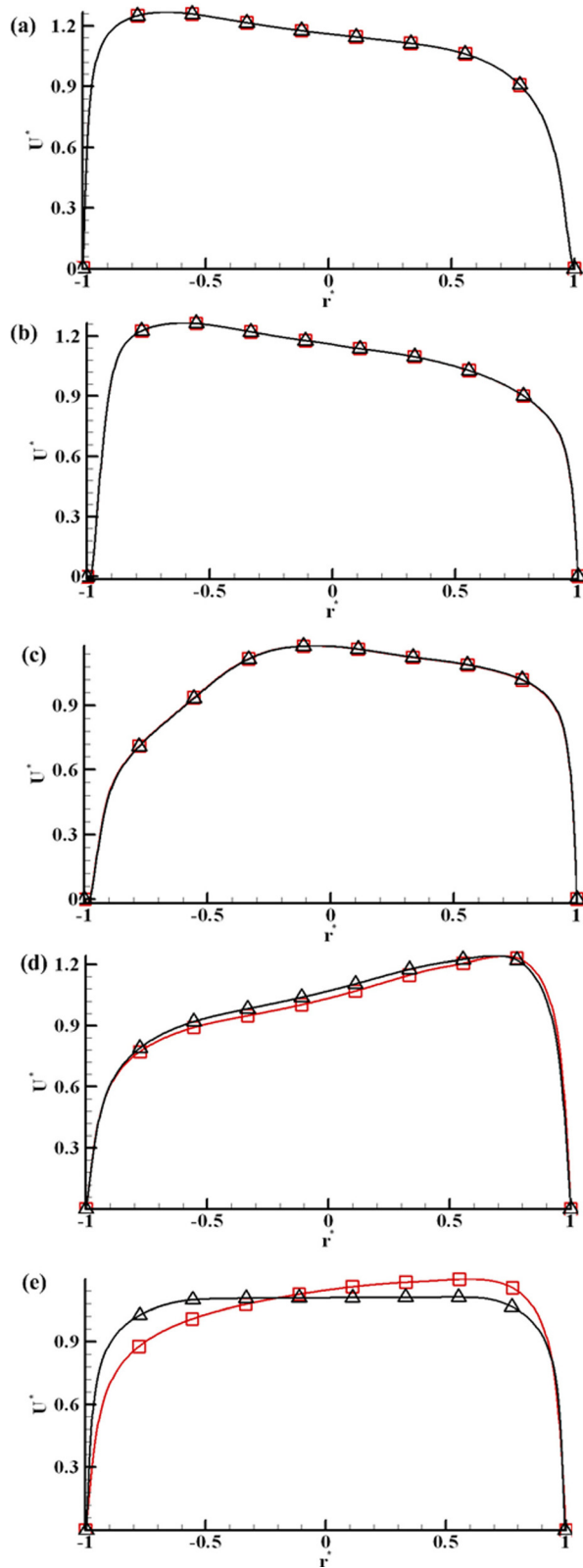
OCTOBER 2014, Vol. 136 / **101203-9**

Fig. 17 Radial distribution of U^* in the 30 deg/30 deg pipe without (squares) and with (triangles) a nozzle at the following five locations along the pipe: (*a*) $s = 0^-$, (*b*) $\varphi_1 = 30$ deg, (*c*) $\varphi_2 = 30$ deg, (*d*) $s = 4.032$, and (*e*) $s = 8.3375$

Fig. 18 Radial distribution of U^* between the 60 deg/60 deg pipe without (squares) and with (triangles) a nozzle at the following five locations along the pipe: (*a*) $s = 0^-$, (*b*) $\varphi_1 = 60$ deg, (*c*) $\varphi_2 = 60$ deg, (*d*) $s = 4.032$, and (*e*) $s = 8.3375$

pipes. The velocity magnitude decreases as the fluid passes through the first bend and the velocity distribution for the 90 deg /90 deg pipe is more complicated compared to that for the 30 deg /30 deg and 60 deg /60 deg pipes. For example, unlike
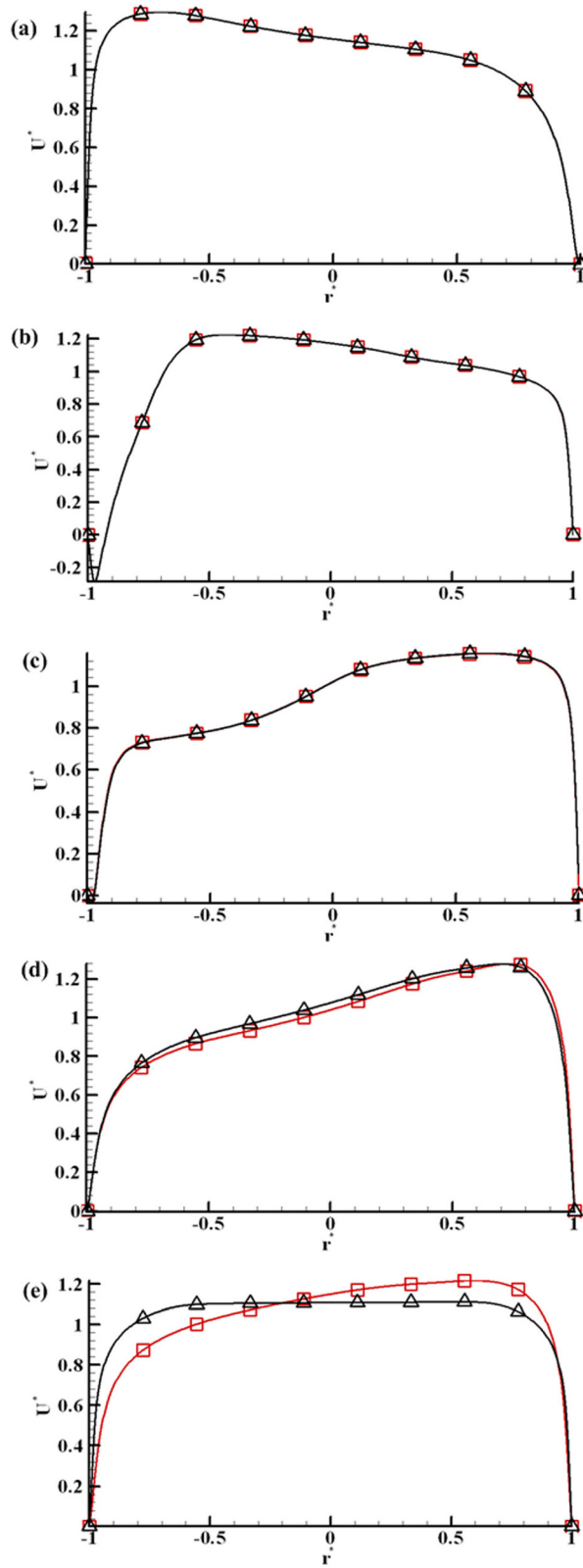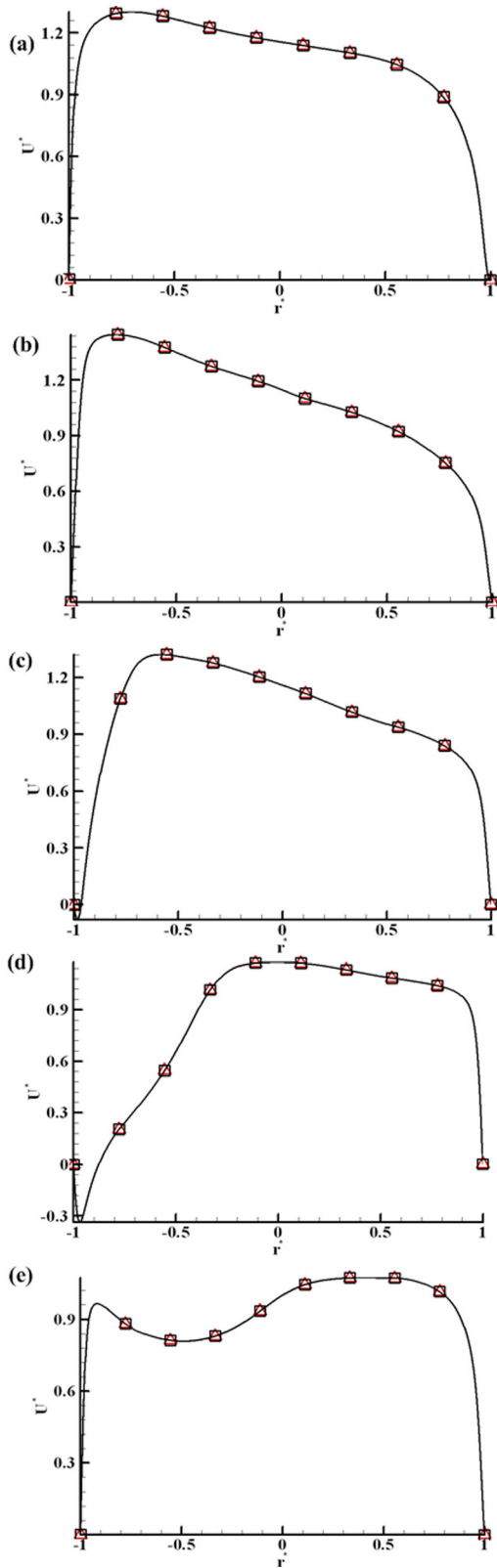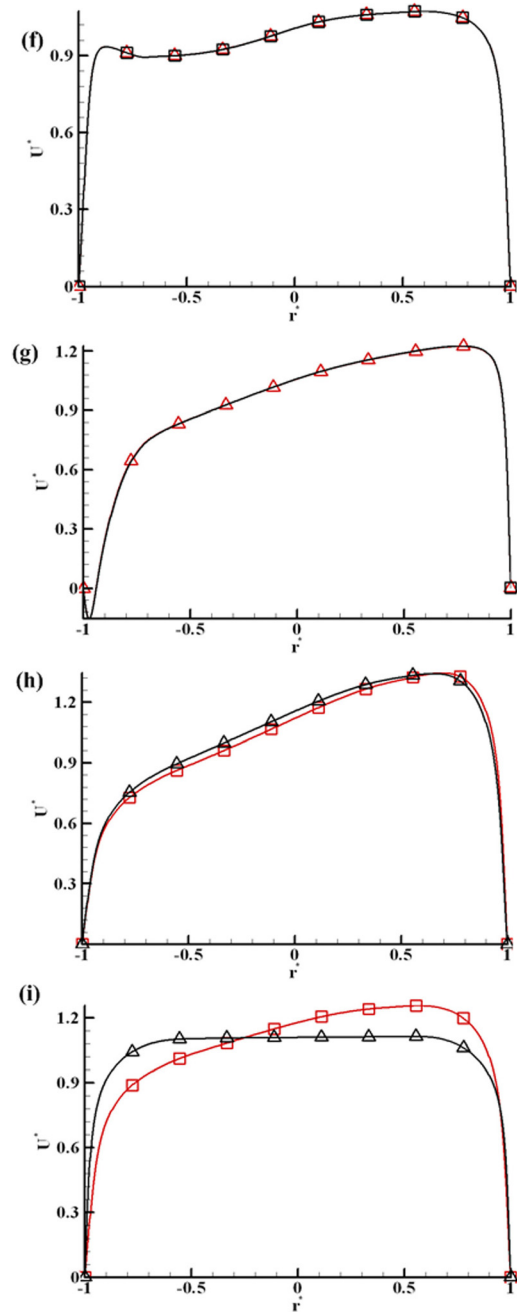
the latter, which show a monotonic distribution in the interior, the former shows an oscillating flow pattern (see Fig. 15). For locations after $\varphi_1 = 30$ deg, we observe that the maximum velocity magnitude has shifted to the vicinity of $r^* = 1$.

Fig. 19 Radial distribution of U^* between the 90 deg/90 deg pipe without (squares) and with (triangles) a nozzle at the following five locations along the pipe: (a) $s = 0^-$, (b) $\varphi_1 = 30$ deg, (c) $\varphi_1 = 60$ deg, (d) $\varphi_1 = 90$ deg, and (e) $\varphi_2 = 0$ deg

Fig. 20 Radial distribution of U^* between the 90 deg/90 deg pipe without (squares) and with (triangles) a nozzle at the following four locations along the pipe: (f) $\varphi_2 = 30$ deg, (g) $\varphi_2 = 90$ deg, (h) $s = 4.032$, and (i) $s = 8.3375$

The presence of a nozzle at the exit of the straight pipe does not significantly affect the radial distribution of the axial velocity (see Fig. 16). At $s = 0^-$, the effect is totally negligible, whereas some

small (insignificant) effects can be observed at $s = 4.032$ and $s = 8.3375$.

For the 30 deg /30 deg pipe (see Fig. 17), the nozzle does not significantly affect the velocity distribution until at the end of the pipe ($s = 8.3375$), at which location the nozzle tends to flatten the velocity distribution in the interior. Similar observations were made for the 60 deg /60 deg (see Fig. 18), and 90 deg /90 deg (see Figs. 19 and 20) pipes. Also common to all curved pipes is the observation of some back flows (negative U^*) that appear after the first bend. The magnitude of the back flow increases with the increasing half-bend angle. However, in all cases, the back flow has disappeared by the time the flow reaches the location $s = 4.032$. Because of the bend, the flow loses kinetic energy,

leading to an increase in the static pressure and, hence, an adverse pressure gradient. The 90 deg /90 deg pipe loses more energy than the 30 deg /30 deg and 60 deg /60 deg pipes. Therefore, the 90 deg /90 deg pipe shows a larger magnitude for the reverse flow.

5 Conclusion

The objective of this study is to comparatively evaluate various pipe configurations that have been proposed for liquid target delivery in the Muon Collider project. The desirable configurations are those that lead to the weakest turbulence intensity levels and uniform momentum thickness at the exit plane. Eight pipe configurations with different half-bend angles are studied, without and with nozzles at the exit region of the pipes. A simple analytical study is performed to describe the laminar flow in curved pipes, in relation to the terms representing curvature effects. The realizable $k - \varepsilon$ (RKE) RANS model has been applied to simulate turbulent flows in the pipes. At the exit plane of the pipe without a nozzle, δ_θ is smaller at $\theta = 0$ deg relative to the value at $\theta = 180$ deg (see Fig. 9), where a lower level of turbulence intensity occurs. The effects of the nozzle include the azimuthal homogenization of the flow and, hence, a uniform velocity, and a corresponding uniform azimuthal distribution of δ_θ. The nozzle also significantly reduces the turbulence intensity at the pipe exit. However, the straight pipe has the least turbulence intensity because of the absence of secondary flows. From the effects of the half-bend angles and nozzles shown in this study, a straight pipe with a convergent nozzle was found to give the weakest turbulence intensity level at the exit plane.

Acknowledgment

Nomenclature

De = Dean number
D_c^* = curvature terms in the continuity equation
D_r^* = curvature terms in the r-momentum equation
$D_{\tilde{z}}^*$ = curvature terms in the $\tilde{z}$-momentum equation
D_θ^* = curvature terms in the θ-momentum equation
I = turbulence intensity (%)
k = turbulence kinetic energy (m^2/s^2)
l^* = nondimensional turbulent characteristic length
L_c = continuity equation for flow in a curved pipe
$\tilde{L}_c$ = continuity equation for flow in a straight pipe
L_{M_1} = r-momentum equation for flow in a curved pipe
L_{M_2} = θ-momentum equation for flow in a curved pipe
L_{M_3} = z-momentum equation for flow in a curved pipe
$\tilde{L}_{M_1}$ = r-momentum equation for flow in a straight pipe
$\tilde{L}_{M_2}$ = θ-momentum equation for flow in a straight pipe
$\tilde{L}_{M3}$ = z-momentum equation for flow in a straight pipe
s = pseudo coordinate direction
U_b = bulk velocity (m/s)
ν^* = nondimensional kinematic viscosity
ν_t^* = nondimensional eddy viscosity
δ = curvature ratio
δ_θ = momentum thickness (m)
ε = turbulence kinetic energy dissipation (m^2/s^3)

σ_k = turbulent Prandtl number for κ
σ_ε = turbulent Prandtl number for ε
τ^* = nondimensional shear stress tensor
φ = pseudo bend angle coordinate direction

References

[1] Efthymiopoulos, I., 2008, "MERIT—The High Intensity Liquid Mercury Target Experiment at the CERN PS," Proceedings of the IEEE NSS'08, p. 3302.

[2] Kirk, H. G., Tsang, T., Efthymiopoulos I., Fabich A., Haug F., Lettry J., Palm M., Pereira H., Mokhov N., Striganov S., Carrol A. J., Graves V. B., Spampinato P. T., McDonald K. T., Bennett J. R. J., Caretta O., Loveridge P., and Park H., 2007, "The MERIT High-Power Target Experiment at the CERN-PS," Proc. of the EPAC08.

[3] Eustice, J., 1910, "Flow of Water in Curved Pipes," Proc. R. Soc.London, Ser. A, **84**(568), p. 107.

[4] Eustice, J., 1911, "Experiments on Stream-Line Motion in Curved Pipes," Proc.R. Soc. London, Ser.A, **85**(576), p. 119.

[5] Dean, W. R., 1927, "Note on the Motion of Fluid in Curved Pipes," Philos. Mag., **20**, p. 208.

[6] Dean, W. R., 1928, "The Streamline Motion of Fluid in a Sinuous Channel," Philos. Mag., **30**, p. 673.

[7] Adler, M., and Angew, Z., 1934, "Perturbation by and Recovery From Bend Curvature of a Fully Developed Turbulent Pipe Flow," J. Math. Mech., **14**, p. 257.

[8] Roew, M., 1970, "Measurements and Computations of Flow in Pipe Bends," J. Fluid Mech., **43**, p. 771.

[9] Enayat, M. M., Gibson, M. M., Taylor, A. M. K. P., and Yianneskis, M., 1982, "Laser-Doppler Measurements of Laminar and Turbulent Flow in Pipe Bend," Int. J. Heat Fluid Flow, **3**, p. 213.

[10] Azzola, J., Humphrey, J. A. C., Iacovides, H., and Launder, B. E., 1986, "Developing Turbulent Flow in a U-Bend of Circular Cross Section: Measurement and Computation," ASME J. Fluids Eng., **108**, p. 214.

[11] Answer, M., So, R. M. C., and Lai, Y. G., 1986, "Perturbation by and Recovery From Bend Curvature of a Fully Developed Turbulent Pipe Flow," Phys. Fluids A, **1**, p. 1387.

[12] Sudo, K., Sumida, M., and Hibara, H., 1998, "Experimental Investigation on Turbulent Flow in a Circular-Sectioned 90-Degree Bend," Exp. Fluids, **25**, p. 51.

[13] Sudo, K., Sumida, M., and Hibara, H., 2000, "Experimental Investigation on Turbulent Flow in a Circular-Sectioned 180-Degree Bend," Exp. Fluids, **28**, p. 42.

[14] Hüttl, T. J., and Friedrich, R., 2000, "Influence of Curvature and Torsion on Turbulent Flow in Helically Coiled Pipes," Int. J. Heat Fluid Flow, **21**, p. 345.

[15] Rudolf, P., and Desova, M., 2007, "Flow Characteristics of Curved Ducts," Appl. Comput. Mech. **1**, p. 255.

[16] Batchelor, G. K., 1967, *An Introduction to Fluid Dynamics*, Cambridge University Press, Cambridge, UK.

[17] Murata, S., Miyake, Y., and Inaba, T., 1976, "Laminar Flow in a Curved Pipe With Varying Curvature," J. Fluid Mech., **73**, p. 735.

[18] Berger, S. A., Talbot, L., and Yao, L. S., 1983, "Flow in Curved Pipes," Annu. Rev. Fluid Mech., **15**, p. 461.

[19] Webster, D. R., and Humphrey, J. A. C., 1997, "Traveling Wave Instability in Helical Coil Flow," Phys. Fluids, **9**, p. 407.

[20] Ladeinde, F., and Torrance, K. E., 1991, "Convection in a Rotating, Horizontal Cylinder With Radial and Normal Gravity Forces," J. Fluid Mech., **228**, p. 361.

[21] Launder, B. E., Reece, G. J., and Rodi, W., 1975, "Modeling the Pressure-Strain Correlation of Turbulence: An Invariant Dynamical Systems Approach," J. Fluid Mech., **68**, p. 537.

[22] Spalart, P. R., and Allmaras, S. R., 1992, "A One Equation Turbulence Model for Aerodynamic Flows," Paper No. AIAA92-0439, p. 439.

[23] Harlow, F. H., and Nakayama, P. I., 1968, "Transport of Turbulence Energy Decay Rate," Los Alamos Scientific Laboratory, Report No. LA3854.

[24] Shih, T. H., Liou, W. W., Shabbir, A., Yang, Z., and Zhu, J., 1995, "A New $k-\varepsilon$ Eddy Viscosity Model for High Reynolds Number Turbulent Flows–Model Development and Validation," Comput. Fluids, **24**(3), p. 227.

[25] Michalke, A., 1965, "On Spatially Growing Disturbances in an Inviscid Shear Layer," J. Fluid Mech., **23**, p. 521.

[26] Plaschko, P., 1979, "Helical Instabilities of Slowly Divergent Jets," J. Fluid Mech., **92**, p. 209.

[27] Cohen, J., and Wygnanski, I., 1987, "The Evolution of Instabilities on the Axisymmetric Jet. Part 1. The Linear Growth of Disturbances Near the Nozzle," J. Fluid Mech., **176**, p. 191.

[28] Corke, T. C., Shakib, F., and Nagib, H., 1991, "Mode Selection and Resonant Phase Locking in Unstable Axisymmetric Jets," J. Fluid Mech., **223**, p. 253.

[29] Corke, T. C., and Kusek, S. M., 1993, "Resonance in Axisymmetric Jets With Controlled Helical-Mode Input," J. Fluid Mech., **249**, p. 307.